Journal of Alloys and Compounds 774 (2019) 299–314

Contents lists available at ScienceDirect

Journal of Alloys and Compounds

journal homepage: http://www.elsevier.com/locate/jalcom

Electronic, optical, elastic, thermoelectric and thermodynamic properties of the spinel oxides $ZnRh_2O_4$ and $CdRh_2O_4$

A. Bouhemadou [a, *], D. Allali [b], K. Boudiaf [a], B. Al Qarni [c], S. Bin-Omran [c], R. Khenata [d], Y. Al-Douri [e, f, g]

[a] Laboratory for Developing New Materials and their Characterizations, Department of Physics, Faculty of Science, University Ferhat Abbas Setif 1, Setif 19000, Algeria
[b] Department of Physics, Faculty of Science, University Mohamed Boudiaf M'sila, 28000 M'sila, Algeria
[c] Department of Physics and Astronomy, College of Science, King Saud University, P.O. Box 2455, Riyadh 11451, Saudi Arabia
[d] Laboratoire de Physique Quantique de la Matière et de Modélisation Mathématique (LPQ3M), Université de Mascara, 29000, Algeria
[e] Nanotechnology and Catalysis Research Center (NANOCAT), University of Malaya, 50603 Kuala Lumpur, Malaysia
[f] Physics Department, Faculty of Science, University of Sidi-Bel-Abbes, 22000, Algeria
[g] Department of Mechatronics Engineering, Faculty of Engineering and Natural Sciences, Bahcesehir University, 34349 Besiktas, Istanbul, Turkey

ARTICLE INFO

Article history:
Received 18 June 2018
Received in revised form
4 September 2018
Accepted 25 September 2018
Available online 29 September 2018

Keywords:
pinel oxides
First-principles calculations
Optoelectronic properties
Elastic constants
Thermoelectric parameters
Thermodynamic properties

ABSTRACT

Density functional FP-LAPW+lo method calculations were performed to explore the structural, electronic, optical, elastic, thermoelectric and thermodynamic properties of the spinel oxides $ZnRh_2O_4$ and $CdRh_2O_4$. The exchange-correlation potential were described using the GGA-PBEsol and TB-mBJ functionals. As the first step, the optimized structural parameters, including the lattice parameter and atomic coordinates, were determined. Electronic band structure, atomic-resolved *l*-projected densities of electronic states and photon energy dependence of the linear optical functions were computed. It is found that both investigated compounds are indirect band gap semiconductors. The band gap results from the splitting of the $Rh : 4d^6$ states into occupied $Rh : 4d - t_{2g}^6$ states, which form the valence band maximum (VBM), and the empty states $Rh : 4d - e_g^0$, which form the conduction band minimum (CBM), owing to the octahedral substantial crystal-field. The electronic interband transitions responsible of the structures in the optical spectra were specified. Single-crystal and polycrystal elastic moduli, wave sound velocities, Debye temperature, Pugh's indicator and indexes of elastic anisotropy were numerically estimated using total energy versus strain. FP-LAPW+lo band structure in combination with the standard Boltzmann transport theory were employed to calculate the thermoelectric parameters, including Seebeck coefficient, electrical and thermal conductivities and figure of merit. It is found that the title compounds are potential candidates for thermoelectric applications if one can further reduce their thermal conductivities via some techniques. FP-LAPW+lo approach in combination with the quasi-harmonic Debye model was employed to study temperature and pressure dependences of some macroscopic physical parameters. Our obtained results in the present work are discussed in comparison with the available experimental and theoretical data. The calculated results show a good agreement with the available experimental and theoretical results.

1. Introduction

Transparent conducting oxides (TCOs) form an exceptional family of materials, possessing two important physical properties together: (i) high optical transparency to visible light and (ii) high electrical conductivity carrier concentrations [1]. Owing to these properties, the TCOs are technologically classed as an important class of materials in the field of optoelectronics [2]. TCOs have found a wide variety of technological applications, such as blue or ultraviolet light emitting diodes (LEDs), solar cells, flat-panel displays, liquid crystal displays, energy-conserving windows, smart windows, touch screens, light emitting displays, invisible security circuits, and dimming rear-view mirrors [2,3]. Most of the TCOs

* Corresponding author.
E-mail addresses: a_bouhemadou@yahoo.fr, abdelmadjid_bouhemadou@univ-setif.dz (A. Bouhemadou).

https://doi.org/10.1016/j.jallcom.2018.09.338
0925-8388/

possess *n*-type conductivity and the development of efficient *p*-type TCOs is one of the main objectives of researchers. High-conductivity *p*-type TCOs comparable with the high performance *n*-type TCOs would be a major breakthrough, enabling advanced devices and applications [4].

Spinel oxides have been identified as promising *p*-type transparent conducting oxide semiconductors [5], which can be an alternative to the *n*-type tin-doped indium oxide (commonly called tin-indium-oxide or ITO) [2]. The perspectives of usage of the spinel oxides as *p*-type transparent conducting oxide semiconductors and for other applications have stimulated extensive experimental and theoretical studies on this exciting class of materials [2,4–20]. Spinel oxides are characterized by their robust properties, such as high melting temperature, high strength, high resistance to chemical attack, large fundamental band gap and good electrical conductivity [12].

The spinel oxides $ZnRh_2O_4$ and $CdRh_2O_4$ are promising transparent semiconducting for various technological applications, such as transparent "metallic" electrodes for solar cells and flat panel displays, including liquid crystal displays (LCDs), and organic light-emitting diodes (OLEDs) [7,15]. The perspectives of usage of the spinel rhodates $ZnRh_2O_4$ and $CdRh_2O_4$ in the optoelectronics field have attracted the interest of some experimental and theoretical researchers [2,4–11,14–17,20–22]. The spinel oxides $ZnRh_2O_4$ and $CdRh_2O_4$ were synthesized and their crystalline structure identified a long time ago [21,22]. Some of the fundamental physical properties of $ZnRh_2O_4$ and $CdRh_2O_4$, such as structural and electronic properties, have been already investigated experimentally [4–11] and theoretically via first-principles calculations [2,4,14–17,20]. However, some other fundamental properties, such as elastic ($ZnRh_2O_4$), thermodynamic, optical ($CdRh_2O_4$) and transport properties have not yet been addressed.

For optoelectronic applications, it is very necessary to accurately determine the electronic and optical properties of the involved materials. Therefore, the first objective of the present work is a precise determination of the parameters characterizing the optoelectronic properties of the title materials. For optoelectronic applications, the involved materials are generally grown in form of thin films on substrates. The lattice mismatch and difference in the thermal expansion coefficients between the grown layers and substrates could cause large stresses in the epitaxial layers, which could affect their fundamental properties. Therefore, it becomes requisite to evaluate their elastic constants, which characterize the response of materials to applied stress. Thus, the second main objective of the present work is a precise estimation of the elastic constants and their related properties for the examined compounds. On the other hand, it is worthy to note that the reported theoretical findings for $ZnRh_2O_4$ and $CdRh_2O_4$ [2,4,14–17,20] were carried out only for the case of zero temperature, i.e., without including any thermal effect. Therefore, because of the not negligible effects of temperature and pressure on the physical properties of materials, the third main objective of the present work is an estimation of temperature and pressure dependences of the lattice parameter, bulk modulus, volume thermal expansion, isochoric and isobaric heat capacities and Debye temperature of the title compounds. Investigation of the thermoelectric performance of the studied compounds constitutes the fourth objective of the present study. Here, we carried out a first-principles study of some physical properties of the spinel oxides $ZnRh_2O_4$ and $CdRh_2O_4$ using the full potential linearized augmented plane wave plus local orbitals method in the framework of density functional theory. Our results cover the optimized structural parameters, electronic bands, charge-carrier effective masses, total and partial densities of electronic states, photon energy dependence of the linear optical functions, elastic moduli and their related properties, temperature and pressure dependences of some macroscopic physical parameters and thermoelectric performances of the $ZnRh_2O_4$ and $CdRh_2O_4$ compounds.

2. Computational details

All performed first-principles calculations in the present work were carried out by means of the full potential linearized augmented plane wave plus local orbitals (FP-LAPW+lo) method [23] as implanted in the WIEN2k code [24]. In the FP-LAPW+lo method, the wave functions are expanded in a linear combination of radial atomic functions and their energy derivatives multiplied by spherical harmonics inside non-overlapping spheres centered at the atomic sites (called muffin-tin spheres; MTS) of radius R_{MT} and in plane wave basis set in the remaining space of the unit-cell (called interstitial region; RI). The R_{MT} were taken as large as possible without overlap between the MTS and to ensure that no core-charge leakage out of the MTS. The wave functions in the IR were expanded in a plane wave basis set with a cut-off parameter $R_{MT}^{\min} K_{\max}$ equal to 9, where $R_{MT}^{\min}$ is the smallest muffin-tin radius and K_{max} is the maximum plane wave vector in the *k*-space. The integration over the Brillouin zone was replaced by a summation on a Monkhorst-Pack grid of $10 \times 10 \times 10$ *k*-points [25]. The self-consistent field iteration process was repeated until the calculated total energy of the crystal converged to less than $10^{-5} Ry$. and the maximum force on any atom was smaller than 0.5 mRy/a.u. (*a.u.*: atomic unit). For the structural, elastic and thermodynamic properties, the electronic exchange-correlation (XC) effects were described using the generalized gradient approximation (GGA) as parameterized by Perdew et al. (the so-called GGA-PBEsol or GGA08) [26]. For the electronic and optical properties, in addition to the GGA08, we adopted the TB-mBJ (Tran-Blaha modified Beck-Johnson) scheme to model the XC effects [27–29]. The TB-mBJ approach is quite successful in reproducing the experimental band gap [29–32].

The energy bands ($E(\mathrm{k})$) were extracted from the DFT calculations. The optical properties were calculated using the optical package of the WIEN2k code. The imaginary part ($\varepsilon_2(\omega)$) of the dielectric function ($\varepsilon(\omega)$;$\varepsilon(\omega) = \varepsilon_1(\omega) + \mathrm{i}\varepsilon_2(\omega)$) was derived from the first-principles calculations by summing over all contributions of the direct electronic transitions from the occupied states in the valence band to the unoccupied states in the conduction band; the indirect and intraband transitions are ignored. The real part ($\varepsilon_1(\omega)$) of the dielectric function was calculated from $\varepsilon_2(\omega)$ using the Kramers-Kronig transformation. All-important linear optical functions, including absorption coefficient $\alpha(\omega)$, refractive index $n(\omega)$, extinction coefficient $k(\omega)$, reflectivity coefficient $R(\omega)$ and electronic loss-energy function $L(\omega)$, were calculated from $\varepsilon_1(\omega)$ and $\varepsilon_2(\omega)$ using the well-established relationships [33].

Knowledge of the elastic constants C_{ij}s of solids (both experimentally and theoretically) is very important as the C_{ij}s characterize the response of solids to external stresses within the elastic limit and are related to many fundamental physical properties of solids. Therefore, it becomes of great importance to determine the C_{ij}s with accuracy. Accurate single-crystal elastic constants C_{ij}s can be obtained from first-principles calculations of the variation of the unit cell total energy as a function of specific lattice distortions. For a cubic system, three different distortions of the optimized unit cell are required to calculate the three independent elastic constants: C_{11}, C_{12} and C_{44}. To check the reliability of the numerical estimation of the C_{ij}s for the considered compounds, two different sets of deformations were applied to the ground state unit cell. Theoretical details of these two different sets of distortion patterns to calculate the C_{ij}s, which were developed by Chapin and Morteza, are given in

Ref. [24].

Transport properties of the considered compounds were calculated using Boltzmann's transport theory within the constant scattering time approximation (CSTA) and the rigid band approximation (RBA) as implemented in the BoltzTraP program [34,35] to shed some light on their thermoelectric performance. A dense *k*-mesh of $50 \times 50 \times 50$ *k*-points in the Brillouin zone was used to calculate the optical, density of states and thermoelectric properties.

3. Results and discussion

3.1. Structural properties

The spinel oxides ARh_2O_4 (A = Zn, Cd) crystalize in a face centered cubic lattice with the $Fd\bar{3}m$(n. 227) space group symmetry. A unit cell of $ZnRh_2O_4$ is depicted in Fig. 1. The ARh_2O_4 unit cell contains 56 atoms or eight unit formulas (8 ARh_2O_4). There are eight A (A = Zn, Cd) cations, 16 Rh cations and 32 O anions in the unit cell, which are located at the Wyckoff positions: 8*a* (1/8, 1/8, 1/8), tetrahedra sites, 16*d* (1/2, 1/2, 1/2), octahedral sites, and 32*e* (u, u, u), respectively. Every atom A (A = Zn, Cd) is surrounded by four O atoms, forming a regular tetrahedron and every atom Rh is surrounded by six O atoms, forming a regular octahedron. The RhO_6 octahedron and AO_4 tetrahedron are connected to each other through common edges. The ARh_2O_4 compounds are characterized by two free structural parameters that are not fixed by the symmetry: (i) the lattice parameter (a) and (ii) the internal coordinate u, which governs the O atom position. At the first step in the present work, full structural optimizations of the considered compounds were performed to determine their equilibrium structural parameters, including the lattice parameter (a) and the internal coordinate (u). To do that, total energy was calculated for a series of primitive cell volumes, where the atomic positions were allowed to relax for each volume. The resulting total energy-volume curve was fitted to the Birch-Murnaghan equation of state [36] to determine the equilibrium primitive cell volume, bulk modulus B and its pressure derive B'. The optimized structural parameters using the GGA08, GGA96 [37] and LDA [38] are listed in Table 1 along with the available experimental and theoretical data. From Table 1, one appreciates the remarkably excellent agreement between the GGA08 optimized lattice parameter value and the corresponding experimental one. The relative deviation (d(%)) of the calculated lattice parameter ($a_{Optimized}$) from the measured ($a_{Measured}$) one, defined as: $d(\%) = ((a_{Optimized} - a_{Measured})/a_{Measured}) \times 100$), is less than 0.7% (0.4%) in the case of $ZnRh_2O_4$ ($CdRh_2O_4$). All investigated properties were calculated at the optimized structural parameters obtained via the GGA08. One can note that the lattice parameter of ARh_2O_4 increases as we go from Zn to Cd due to the increase of the ionic radii.

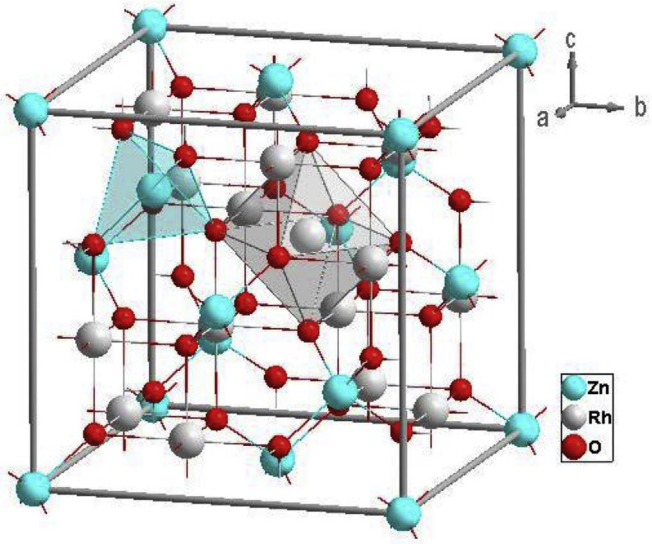

Fig. 1. One unit cell of $ZnRh_2O_4$. Coordination polyhedra around the Zn and Rh atoms are shown: four O atoms, forming a regular tetrahedron, surround every Zn atom and six O atoms, forming a regular octahedron, surround every Rh atom.

Table 1
Calculated equilibrium lattice parameter (a_0, in Å), internal coordinate of the oxygen atom (u), bulk modulus (B, in GPa) and pressure derivative of the bulk modulus (B') for $ZnRh_2O_4$ and $CdRh_2O_4$ along with the available experimental and theoretical results in the literature.

	$ZnRh_2O_4$			$CdRh_2O_4$		
	Present	Expt.	Others	Present	Expt.	Others
a_0	8.5038 [1]	8.506 [a]	8.57 [c]	8.7700 [1]	8.73 [e]	8.790 [g]
	8.6233 [2]	8.489 [b]	8.48 [c]	8.8939 [2]	8.722 [f]	
	8.4161 [3]	8.482 [b]	8.49 [d]	8.6836 [3]		
u	0.26049 [1]	0.263 [b]	0.260 [d]	0.26829 [1]		
	0.25967 [2]			0.26851 [2]	0.264 [g]	
	0.26016 [3]			0.26828 [3]		
B_0	197.88 [1]	198.19 [h]		186.89 [1]		
	173.85 [2]			164.55 [2]		
	219.94 [3]			206.13 [3]		
B'	5.13 [1]			4.97 [1]		
	5.15[2]			4.94 [2]		
	5.12 [3]			5.01 [3]		

[1]Present: using the GGA08;[2] Present: using the GGA96;[3] Present: using the LDA.
[a] Ref. [21];
[b] Ref. [9];
[c] Ref. [2];
[d] Ref. [17];
[e] Ref. [22];
[f] Ref. [11];
[g] Ref. [15];
[h] Ref. [16].

3.2. Electronic properties

The computed electronic energy band dispersions for the optimized crystal structures of the title compounds along the selected high-symmetry lines within the BZ using the GGA08 and TB-mBJ are depicted in Fig. 2. As it can be seen from Fig. 2, both studied spinels are indirect band gap semiconductors, where the valence band maximum (VBM) is located at the X point in the BZ while the conduction band minimum (CBM) is located near the X point along the $X \rightarrow \Gamma$ line. The main features (band dispersions) of the GGA08 and TB-mBJ band structures are practically the same, except that the TB-mBJ band gap is much larger than the GGA08 one. The GGA08 band gap sizes for $ZnRh_2O_4$ and $CdRh_2O_4$ are 0.87 eV and 0.81 eV, respectively. The GGA08 band gap for $ZnRh_2O_4$ is severely underestimated compared to the measured one, which ranges from 2.0 eV to 2.74 eV [4–7,9]. Experimental band gap for $CdRh_2O_4$ is not yet available. The TB-mBJ band gaps of $ZnRh_2O_4$ and $CdRh_2O_4$ are 2.54 eV and 2.48 eV, respectively. One appreciates that the TB-mBJ potential improves significantly the opening of the band gap. The calculated fundamental band gap of $ZnRh_2O_4$ using the TB-mBJ potential, which is 2.54 eV, compares very well with the available experimental values, which range from 2.0 eV to 2.74 eV [4–7,9]. Thus, one can state that TB-mBJ provides a reliable simple method that can be a viable alternative to the computationally expensive approaches for the calculation of band gaps with an acceptable accuracy. It is worthy to note that the discrepancy between

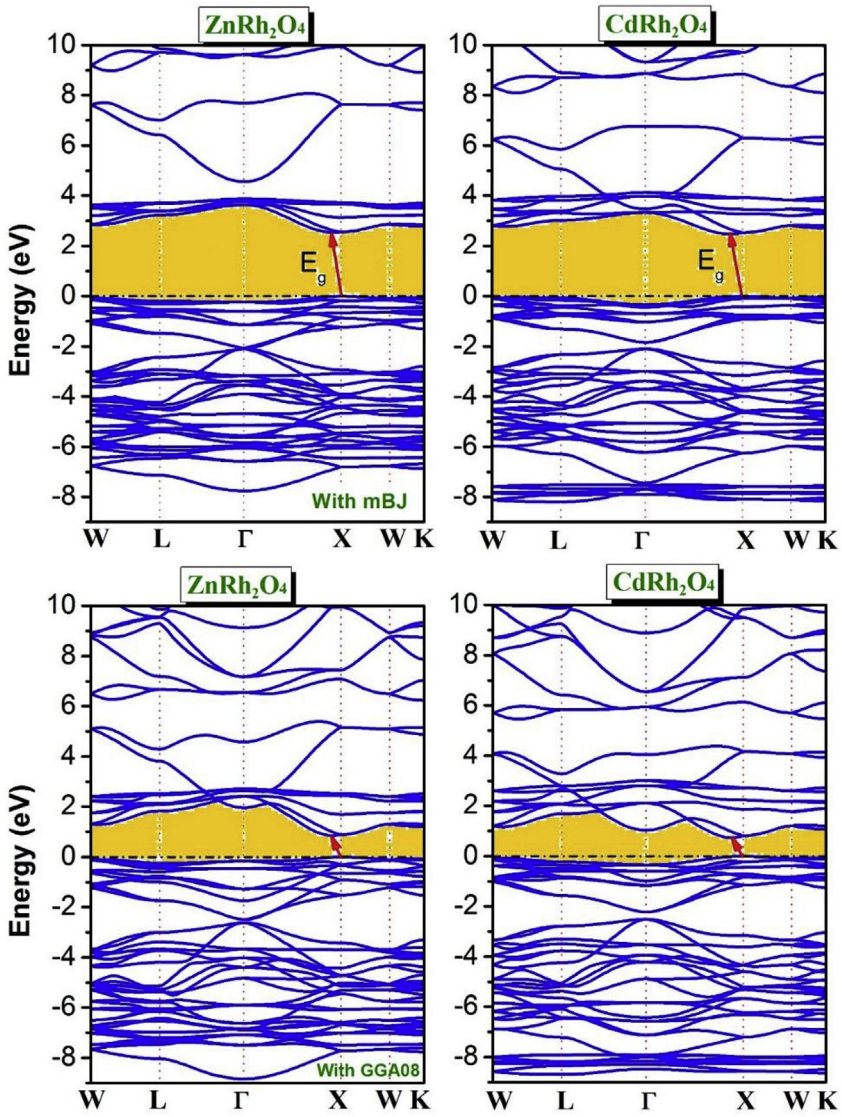

Fig. 2. Calculated band structures for $ZnRh_2O_4$ and $CdRh_2O_4$ using the GGA08 and TB-mBJ. The Fermi level is set to zero energy. Conduction-band minimum occurs near X-point along the X-Γ direction in the BZ.

experimental data reported by different researcher groups for the $ZnRh_2O_4$ band gap is probably due to the experimental errors that usually arises from the used measurement technique and sample quality. In addition, this discrepancy between experimental data can be explained by the fact that the band gap value depends on the temperature at which the measurement is done. Our calculated band gaps using the GGA08 are consistent with the earlier reported theoretical results (Table 2) using the standard LDA and GGA methods [2,16]. Our TB-mBJ band gaps are also consistent with the earlier reported theoretical results using the TB-mBJ and hybrid functionals (sX-LDA) [15,16,20]. It might be worth mentioning that the minor differences between our TB-mBJ band gaps and the earlier reported results using TB-mBJ could be attributed to the fact that these values are derived from calculations performed at slightly different values of the equilibrium structural parameters; the band gap value is sensitive to the structural parameter values. One can note the downward trend of the fundamental band gap when moving from $ZnRh_2O_4$ to $CdRh_2O_4$ in accordance with the electronegativity trend.

Qualitative information about the ability of the studied compounds to easily conduct electricity can be obtained from the analysis of the energy band dispersions at the energy band extremes. Fig. 2 shows that the valence energy bands around the VBM

Table 2
Calculated fundamental band gaps (E_g, in eV unit) for $ZnRh_2O_4$ and $CdRh_2O_4$ along with the available theoretical and experimental findings.

	E_g
$ZnRh_2O_4$	
Present	
Using GGA08	0.85
Using TB-mBJ	2.54
Expt.	2.0–2.74 [4–7,9]
Others	2.53[20], 2.88[20], 3.33[2]
	0.897[16], 2.509 [16], 1.65 [4]
	0.80[2], 2.87[2]
$CdRh_2O_4$	
Present	
Using GGA08	0.74
Using TB-mBJ	2.48
Others	1.065 [15], 2.623 [15]

are less dispersive than the conduction bands around the CBM, which indicate that the effective mass of the hole will be heavier than that of the electron. This result suggests that the *p*-doped $ZnRh_2O_4$ and $CdRh_2O_4$ compounds should be more favourable for thermoelectric performance than the *n*-doped ones, while the electrical conductivity by conduction band electrons should be more favourable than that by valence band holes.

Transport properties in semiconductors are principally controlled by the effective masses of charge-carriers. Therefore, it becomes necessary to evaluate the electron and hole effective masses of the investigated compounds at the band edges. To calculate the hole effective mass m_h^* (electron effective mass m_e^*), we first fit the dispersion (E(k)) of the topmost valence band (lowest conduction band) around the VBM (around the CBM) to a quadratic polynomial in the reciprocal lattice vector $\vec{k}$(E(k) $= Ak^2$), then the effective mass m* (in unit of m_0, where m_0 denotes the electron rest mass) can be estimated using the following expression: $\frac{1}{m^*} = \frac{m_0}{\hbar^2}\frac{\partial^2 E(k)}{\partial^2 k}\Big|_{k=k_0}$. Predicted effective masses m_h^* at the VBM and m_e^* at the CBM towards the X→W and X→Γ directions for $ZnRh_2O_4$ and $CdRh_2O_4$ are listed in Table 3. It is apparent that both m_h^* and m_e^* exhibit a noticeable dependence on the crystallographic directions. The values of m_h^* and m_e^* towards the X→W direction are larger than the corresponding ones towards the X→Γ direction, suggesting that the mobility of the charge-carries along the X→Γ line should be larger than that along the X→W one. The obtained results show also that the effective mass of the hole in $ZnRh_2O_4$ is more dependent on the crystallographic directions than that of the electron. Hence, the electrical conductivity by holes should be more anisotropic than that by electrons. In addition, the hole effective mass is larger than the electron one, indicating that the hole mobility should be smaller than the electron one in the considered compounds. Therefore, as the electrical conductivity σ is inversely proportional to the charge-carrier mass, one can expect that for the same charge-carrier concentration and temperature, the electrical conductivity σ of the *n*-type doped system should be larger than that of the *p*-type doped one. Moreover, as the Seebeck coefficient *S* is proportional to the effective mass of charge-carrier, one can expect that the *S* of the *p*-type doped system should be larger than that of the *n*-type doped one.

A closer examination of the electronic structure can be obtained by calculating the total density of states TDOS (states/eV/unit-cell) and atomic-resolved *l*-projected density of states PDOS (states/eV/atom/orbital) diagrams. The TDOS and PDOS spectra of the title compounds are illustrated in Fig. 3. The valence bands can be divided into three distinct groups (four groups) for $ZnRh_2O_4$ ($CdRh_2O_4$); V1, V2 and V3 (V1, V2, V3 and V4). For both studied spinels, the lowest energy valence band group (not shown in Fig. 3 for seek of clarity), ranging from approximately −20.8 eV to −19.6 eV, arises from the O: 2*s* orbitals. The V2 valence band group in the TDOS spectrum of $ZnRh_2O_4$, extending from approximately −7.7 eV to −2.1 eV, is originated mainly from the Zn:

Table 3
Calculated electron and hole effective masses at the CBM and VBM, respectively, towards the $X \rightarrow W$ and $X \rightarrow \Gamma$ directions in the Brillouin zone.

$ZnRh_2O_4$				$CdRh_2O_4$			
m_e^*		m_h^*		m_e^*		m_h^*	
$\sim X \rightarrow W$	$\sim X \rightarrow \Gamma$	$X \rightarrow W$	$X \rightarrow \Gamma$	$\sim X \rightarrow W$	$\sim X \rightarrow \Gamma$	$X \rightarrow W$	$X \rightarrow \Gamma$
0.652	0.604	3.092	1.954	0.641	0.187	3.652	2.512

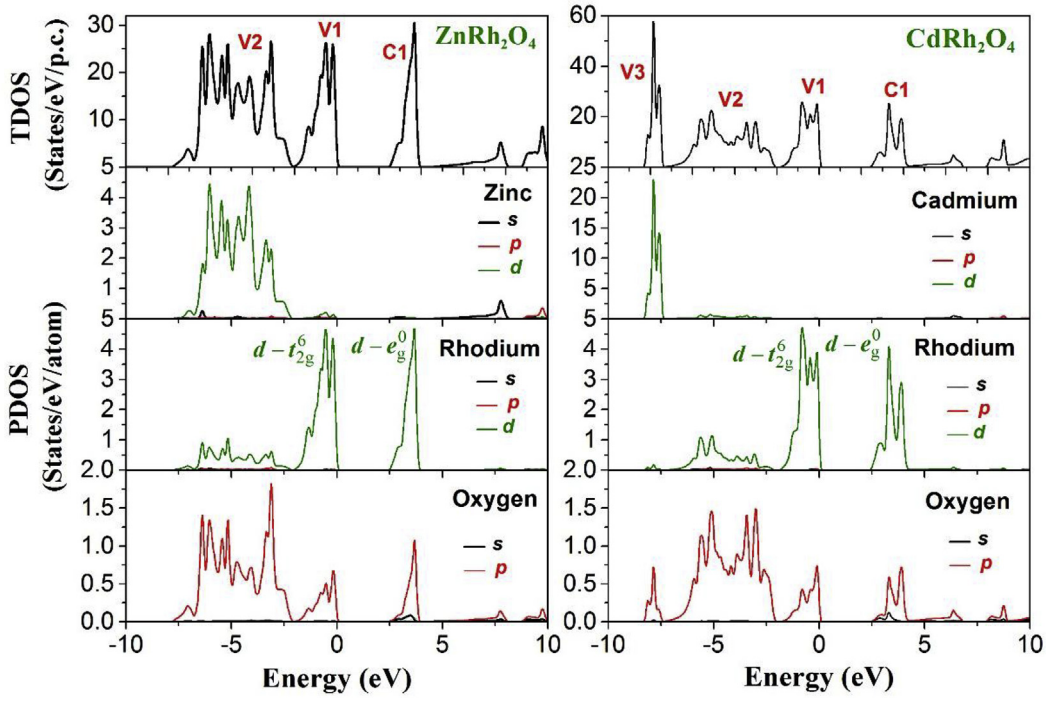

Fig. 3. Calculated total and partial densities of states (TDOS and PDOS) for $ZnRh_2O_4$ and $CdRh_2O_4$. The Fermi level is set to zero. p.c.: primitive cell.

3*d* and O: 2*p* orbitals. For the $CdRh_2O_4$ case, the V3 group, ranging from approximately −8.3 eV to −7.4 eV, consists of the Cd: 4*d* and O: 2*p* states and the V2, ranging approximately from −8.3 to −7.4 eV, is composed of an admixture of the Rh: 4*d* and O: 2*s* orbitals. The upper valence band group, ranging from approximately −1.8 eV to Fermi level for $ZnRh_2O_4$ and from approximately −1.5 eV to Fermi level for $CdRh_2O_4$, is formed from the strongly hybridized occupied $Rh: 4d - t_{2g}^6$ and O: 2*p* states, suggesting a directional covalent bond between the Rh and O atoms. The lowest energy conduction band group (C1) is dominated by the unoccupied $Rh: 4d - e_g^0$ with significant contribution from the O: 2*p* states. The $Rh: 4d^6$ states are separated into occupied $Rh: 4d - t_{2g}^6$ states, which form the VBM, and empty $Rh: 4d - e_g^0$ states, which form the CBM, owing to the octahedral crystal-field splitting [4].

3.3. Optical properties

Fig. 4 depicts the imaginary ($\varepsilon_2(\omega)$) and real ($\varepsilon_1(\omega)$) parts of the dielectric function ($\varepsilon(\omega)$) of the considered compounds. The $\varepsilon_2(\omega)$ spectrum of each considered compound exhibits 10 critical point structures, labelled E_1, E_2… E_{10} in the figure. The behavior of $\varepsilon_2(\omega)$ spectrum is rather similar for $ZnRh_2O_4$ and $CdRh_2O_4$ over the considered range of energy. It is worth to attempt to identify the electronic transitions that are responsible for the $\varepsilon_2(\omega)$ spectrum structures from the calculated band structures. To determine the microscopic origin of the observed peaks, the $\varepsilon_2(\omega)$ spectrum was decomposed into individual contributions from each direct allowed electronic transition from occupied valence state V_i to the unoccupied conduction state C_j ($V_i \rightarrow C_j$). Fig. 5 shows the decomposition of the $\varepsilon_2(\omega)$ spectrum of $ZnRh_2O_4$ into band to band contributions and the dispersion of the transition energy bands $E(k) = E_{C_i}(k) - E_{V_j}(k)$. The positions of the main peaks E_i of the $\varepsilon_2(\omega)$ spectrum and the extended direct inter-band transitions that contribute dominantly to the optical structures and their locations in the Brillouin zone for $ZnRh_2O_4$ are given in Table 4. Based on the TDOS diagram of $ZnRh_2O_4$ ($CdRh_2O_4$), the main contributions to the $\varepsilon_2(\omega)$ spectrum are originated from the electronic direct transitions from the valence band groups V1 and V2 (V1, V2 and V3) to the conduction band group C1. Based on the PDOS spectrum of $ZnRh_2O_4$ ($CdRh_2O_4$), we can conclude that the optical structures E_1, E_2, E_3 and E_4 of the $ZnRh_2O_4$ ($CdRh_2O_4$) $\varepsilon_2(\omega)$ spectrum are originated mainly from the electronic direct transitions from the occupied *Rh*: $4d - t_{2g}^6$ and the O: 2*p* (in a second degree) valence band states to the unoccupied $Rh: 4d - e_g^0$ and O: 2*p* conduction band states. The optical structures E_5, E_6, E_7, E_8, E_9 and E_{10} are resulted from the electronic direct transitions from the $Zn: 3d$ (or $Cd: 4d$) valence bands to the $Rh: 4d - e_g^0$ and $O: 2p$ conduction band states.

The electronic part of the static dielectric constant $\varepsilon(0)$, a parameter of fundamental importance in many aspect of materials science, can be obtained from the low energy limit of the $\varepsilon_1(\omega)$ spectrum, i.e.,$\varepsilon_1(\omega \rightarrow 0)$. The calculated static dielectric constants for $ZnRh_2O_4$ and $CdRh_2O_4$ are respectively equal to 4.262 and 5.126. The $\varepsilon_1(0)$ value of $ZnRh_2O_4$ is lower than that of $CdRh_2O_4$. This result is consistent with Penn model [39]: $\varepsilon_1(0) \approx 1 + (\hbar\omega_p/E_g)^2$, where $\hbar\omega_p$ is the plasma energy, i.e., larger is the band gap smaller is the static dielectric constant $\varepsilon_1(0)$.

Photon energy dependence of the optical complex refractive index $\tilde{n}$ ($\tilde{n} = n + ik$), which is an interesting optical parameter for the design of optoelectronic devices, is presented in Fig. 6 for the two studied compounds. The calculated zero energy ($\hbar\omega = 0; \quad \lambda = \infty$) $n(0)$ value for $ZnRh_2O_4$ ($CdRh_2O_4$) is equal to 2.065 (2.263). The $n(\omega)$ maximum value of $ZnRh_2O_4$ ($CdRh_2O_4$), which is equal to 3.105 (3.242), is produced for a photon energy of about 5.80 eV (~6.24 eV). The maximum value of the extinction coefficient $k(\omega)$, which is equal to 2.534 (2.168), appears for a photon energy of about 6.90 eV (~6.91 eV) for $ZnRh_2O_4$ ($CdRh_2O_4$).

The absorption coefficient $\alpha(\omega)$, which gives the fraction of energy lost by the incident radiation per length unit when it passes through a material, is depicted in Fig. 6. The absorption coefficient $\alpha(\omega)$ of $ZnRh_2O_4$ ($CdRh_2O_4$) stars to increase when the photon energy is higher than the absorption edge and reaches its maximal value $\sim 1.77 \times 10^6$ cm^{-1} ($\sim 1.53 \times 10^6$ cm^{-1}) at approximately 7 eV. This is a typical characteristic of semiconductors and insulators. $ZnRh_2O_4$ ($CdRh_2O_4$) exhibits a noticeable absorption ($> 10^6 cm^{-1}$) in the energy range between 6 eV and 10 eV (6 eV and 8.5 eV).

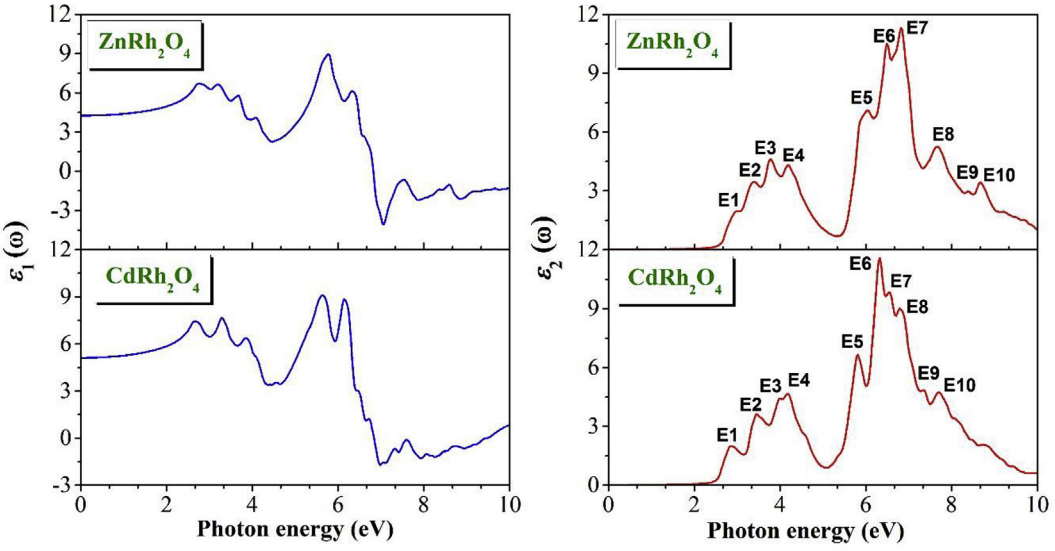

Fig. 4. Calculated real ($\varepsilon_1(\omega)$) and imaginary ($\varepsilon_2(\omega)$) parts of the dielectric function for $ZnRh_2O_4$ and $CdRh_2O_4$. The critical point structures (peaks) are point out by the label E_i (i = 1 to 10).

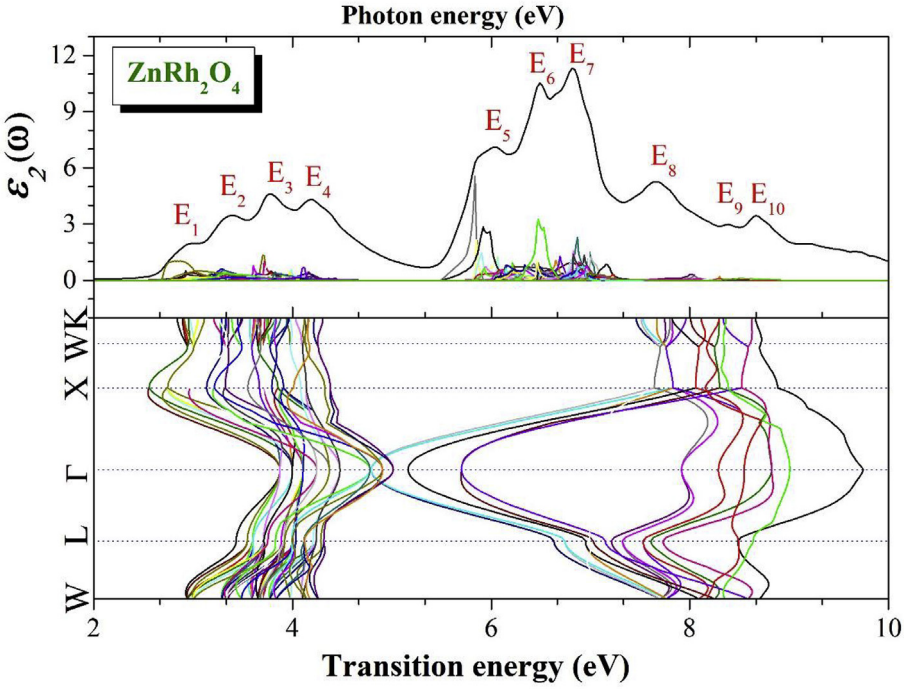

Fig. 5. Decomposition of the imaginary part ($\varepsilon_2(\omega)$) of the dielectric function into band-to-band contributions (top panel) and the transition energy band structure (bottom panel) for the cubic spinel $_{ZnRh2O4}$. The counting of the bands is down (up) from the top (bottom) of the valence (conduction) band.

Table 4
Peak positions of the $\varepsilon_2(\omega)$ spectrum together with the dominant interband transition contributions to every peak and their location in the Brillouin zone for $ZnRh_2O_4$. The counting of the bands is down (up) from the top (bottom) of the valence (conduction) band.

Optical structures		Dominant interband transition contributions			
Structure	Peak position	Transition	Region	Percentage	Energy (eV)
E_1	2.96	(V_1-C_1)	W-L, Γ-X-W-K	25%	2.92
	2	(V_2-C_1)	W-L, Γ-X	19.5%	2.97
		(V_3-C_1)	Γ-X-W	51%	2.82
		(V_4-C_1)	Γ-X-W	9.8%	2.99
E_2	3.38	(V_1-C_3)	Γ-X-W	12.33%	3.26
	3.42	(V_1-C_4)	Γ-X-W	17.49%	3.29
		(V_1-C_5)	W-L	6.98%	3.54
		(V_2-C_3)	W-L, Γ-X-W-K	15.16%	3.29
		(V_2-C_4)	Γ-X-W	9.03%	3.17
		(V_3-C_2)	W-L, Γ-X	3.11%	3.07
		(V_3-C_3)	Γ-X-W-K	6.47%	3.34
		(V_3-C_4)	W-L, Γ-X-W-K	8.25%	3.36
		(V_4-C_2)	W-L, Γ-X, W-K	14.78%	3.04
E_3	3.77	(V_1-C_6)	W-L, X-W-K	17.25%	3.61
	4.55	(V_1-C_7)	W-L, W-K	29.23%	3.49
		(V_1-C_8)	W-L, Γ-X, W-K	5.89%	3.74
		(V_2-C_5)	W-L, X-W-K	7.648%	3.66
		(V_2-C_6)	W-L, X-W-K	4.74%	3.59
		(V_2-C_7)	W-L, X-W-K	21.75%	3.71
		(V_2-C_8)	W-L, Γ-X, W-K	20.65%	3.74
		(V_3-C_5)	W-L, W-K	5.27%	3.64
		(V_3-C_6)	L-Γ, X-W	5.82%	3.74
		(V_4-C_5)	W-L, X-W-K	10.76%	3.79
E_4	4.19	(V_4-C_7)	W-L, Γ-X	3.04%	4.08
	4.27	(V_4-C_8)	W-L, Γ-X	7.96%	4.16
		(V_5-C_3)	W-L, Γ-X	3.51%	3.91
		(V_5-C_4)	W-L, Γ-X	3.25%	3.88
		(V_5-C_5)	W-L	4.51%	3.93
		(V_5-C_6)	W-L, X-W	13.27%	4.0125
		(V_5-C_7)	W-L, W-K	5.38%	4.08
		(V_5-C_8)	W-L, Γ-X	5.15%	4.23
		(V_6-C_5)	W-L	10.11%	3.98
		(V_6-C_6)	W-L	4.07%	4.037
		(V_7-C_3)	Γ-X-W	10.53%	3.81

(*continued on next page*)

Table 4 (*continued*)

Optical structures		Dominant interband transition contributions			
Structure	Peak position	Transition	Region	Percentage	Energy (eV)
		(V_7-C_4)	W-L, Γ-X	2.85%	4.037
		(V_8-C_4)	Γ-X-W	16.15%	4.11
E_5	6.04	(V_{13}-C_2)	W-L, Γ-X-W-K	73.97%	5.86
	7.07	(V_{13}-C_3)	W-L, Γ-X	17.82%	6.06
		(V_{13}-C_4)	W-L- Γ-X	20.60%	5.91
		(V_{13}-C_5)	W-L, Γ-X	10.39%	5.94
		(V_{14}-C_2)	W-L, Γ-X	39.88%	5.91
		(V_{14}-C_6)	W-L, Γ-X	11.17%	6.14
		(V_{14}-C_7)	W-L, Γ-X	9.19%	6.14
		(V_{17}-C_1)	W-L, Γ-X-W-K	7.92%	6.11
		(V_{17}-C_2)	W-L, Γ-X, W	7.07%	6.21
E_6	6.49	(V_{13}-C_8)	L-Γ-X	7.55%	6.14
	10.46	(V_{14}-C_3)	W-L, X-W-K	7.36%	6.21
		(V_{14}-C_4)	W-L, X-W-K	8.88%	6.215
		(V_{17}-C_3)	W-L	8.98%	6.46
		(V_{17}-C_4)	W-K	6.97%	6.48
		(V_{18}-C_1)	L-Γ-X	7.83%	6.34
		(V_{18}-C_3)	W-L-Γ-X-W	10.22%	6.66
		(V_{19}-C_1)	W-L-Γ-X, W-K	8.31%	6.43
		(V_{19}-C_2)	W-L, Γ-X, W-K	9.56%	6.48
		(V_{20}-C_1)	W-L, Γ-X-W	31.07%	6.46
E_7	6.82	(V_{17}-C_5)	W-L-Γ	4.78%	6.61
	11.28	(V_{17}-C_6)	W-L	8.33%	6.80
		(V_{17}-C_7)	W-L-Γ	6.20%	6.90
		(V_{17}-C_8)	W-L-Γ	20.39%	6.85
		(V_{18}-C_4)	W-L-Γ-X	11.25%	6.68
		(V_{18}-C_5)	W-L-Γ, X-W-K	8.51%	6.88
		(V_{19}-C_3)	W-L-Γ-X-W-K	9.72%	6.80
		(V_{19}-C_4)	W-L-Γ-X-W-K	13.82%	6.83
		(V_{19}-C_6)	W-L-Γ	12.23%	6.80
		(V_{20}-C_3)	L-Γ-X-W-K	4.43%	6.85
		(V_{20}-C_4)	L-Γ-X-W-K	6.47%	6.90
		(V_{20}-C_5)	W-L-Γ	6.56%	6.95
E_8	7.66	(V_{18}-C_7)	W-L-Γ, X-W-K	49.04%	7.00
	5.26	(V_{18}-C_8)	W-L-Γ,X-W	24.14%	7.00
		(V_{19}-C_7)	W-L-Γ-X	16.15%	7.15
		(V_{19}-C_8)	W-L-Γ-X-W-K	5.89%	7.23
		(V_{20}-C_6)	W-L-Γ	8.55%	7.00
		(V_{20}-C_7)	L-Γ-X-W-K	5.26%	7.25
E_9	8.39	(V_1-C_{10})	L-Γ-X	10.80%	8.00
	2.93	(V_2-C_{10})	L-Γ-X	7.57%	8.047
		(V_5-C_{10})	Γ-X	0.64%	8.39
		(V_6-C_{10})	W-L-Γ	0.88%	8.21
		(V_7-C_{10})	W-L-Γ, X-W-K	7.36%	8.29
E_{10}	8.67	(V_8-C_{10})	W-L-Γ	2.69%	8.49
	3.34	(V_9-C_{10})	W-L-Γ-X-W	2.96%	8.61
		(V_{11}-C_{10})	W-L-Γ, X-W	1.07%	8.74
		(V_{28}-C_8)	W-L-Γ-X	2.66%	8.44
		(V_{29}-C_8)	W-L, Γ-X	3.59%	8.49

The reflectivity spectra R(ω) of the studied compounds are represented in Fig. 6. The $ZnRh_2O_4$ ($CdRh_2O_4$) R(ω) reaches its maximal value of approximately 50% (40%) at approximately 7 eV in. The electron energy-loss function L(ω), which is an important factor describing the energy loss of fast electrons traversing a homogeneous dielectric material, is plotted in Fig. 6. The L(ω) primary peak location is usually associated with the plasma frequency ω_p. A sharp maximum of the $L(\omega)$ spectrum located at approximately 11.4 eV (9.60 eV) is associated with the plasma oscillations in $ZnRh_2O_4$ ($CdRh_2O_4$). The $L(\omega)$ peak corresponds to the trailing edges in the reflection spectrum.

3.4. Elastic properties

Calculated elastic constants (C_{ij}s) for $ZnRh_2O_4$ and $CdRh_2O_4$ are tabulated in Table 5 along with the theoretical results reported previously for $CdRh_2O_4$. There are no experimental data for the elastic constants for the two studied compounds. Theoretical prediction of the elastic constants are available only for the $CdRh_2O_4$ compound. The good agreement between our elastic constants values for the $ZnRh_2O_4$ and $CdRh_2O_4$ calculated using two different approaches proves the reliability of the obtained results. One can note that our calculated values for C_{11} and C_{12} are somewhat larger than those previously calculated for $CdRh_2O_4$ while the C_{12} value is somewhat smaller than the reported one [15]. It is worth to note also that the previously reported results were obtained using the strain-stress method in the framework of pseudopotential plane wave approach, which is different from the used method in the present work. From Table 5, one can note:

(i) In both studied compounds, the C_{11} value is higher than that of C_{44}, suggesting that the resistance of the studied compounds to unidirectional compression is higher than their resistance to shear deformation.
(ii) Calculated elastic constants C_{ij}s satisfy the Born and Huang mechanical stability criteria [40], suggesting that the examined systems are mechanically stable under elastic strain perturbations.

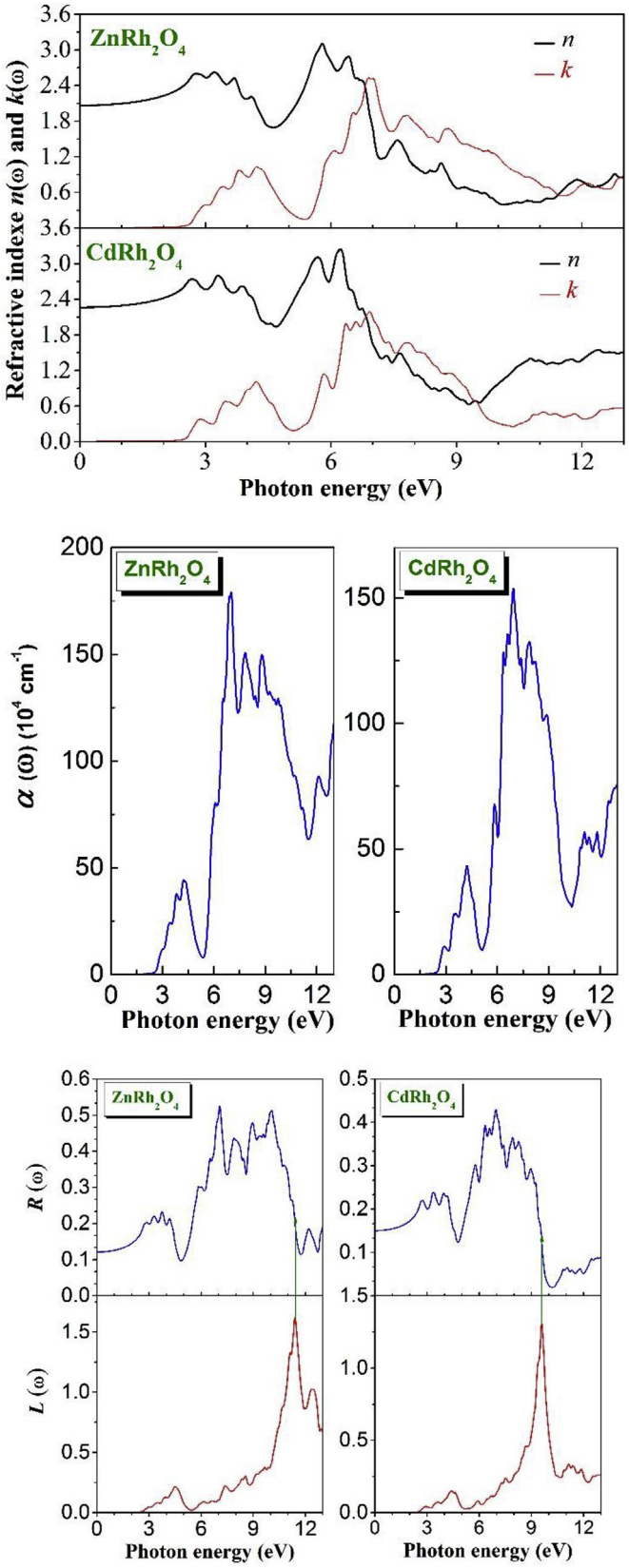

Fig. 6. Calculated refractive index $n(\omega)$, extinction coefficient $k(\omega)$, absorption coefficient $\alpha(\omega)$, reflectivity $R(\omega)$, energy-loss function $L(\omega)$ for $ZnRh_2O_4$ and $CdRh_2O_4$.

Table 5
Calculated elastic constants (C_{11}, C_{12} and C_{44}, in GPa) using Chapin and Morteza methods [24], bulk modulus (B, in GPa); calculated from the relation $B = (C_{11} + 2C_{12})/3$, shear modulus ($G = (G_R + G_V)/2$, in GPa), Young's modulus (E, in GPa), Poisson's ratios (σ), Lame's coefficients (λ and μ, in GPa), Debye temperature θ_D and Pugh ratio B/G for $ZnRh_2O_4$ and $CdRh_2O_4$.

Property	$ZnRh_2O_4$		$CdRh_2O_4$		
	Chapin	Morteza	Chapin	Morteza	Others
C_{11}	271	277	226	240	206.1 [15]
C_{12}	159	168	166	173	112.3 [15]
C_{44}	62	63	53	53	62.5 [15]
B	196	204	186	195	143.5 [15]
G_V	59.6	59.6	43.8	45.2	
G_R	59.45	59.30	40.56	42.99	
$G = \mu$	59.52	59.45	42.18	44.09	55.7 [15]
E	162.2	162.6	117.6	123.0	147.9 [15]
σ	0.3623	0.3673	0.3945	0.3950	0.29 [15]
λ	156.6	164.6	157.8	165.9	
B/G	3.30	3.44	4.409	4.429	2.58 [15]
θ_D	450	450	348	355	396 [15]

(iii) The sound wave velocities in a medium are related to some of its physical properties such as its thermal conductivity. The calculated sound wave velocities propagating along the [100], [110] and [111] cubic crystallographic directions of the investigated systems are gathered in Table 6. The propagation of the longitudinal sound waves is faster along the [100] direction than along the [110] and [111] ones, indicating that the [100] direction is the most rigid one.

(iv) The isotropic polycrystalline elastic constants, such as the bulk modulus B, shear modulus G, Young's modulus E and Poison's coefficient σ, of the considered compounds are estimated from the obtained single-crystal elastic constants C_{ij}s using the Voigt-Reuss-Hill approximation and the obtained results are listed in Table 5. From the computed values of the isotropic moduli, one can note the following:

(a) A good agreement between the bulk modulus value calculated from the C_{ij}s and the corresponding one computed from the EOS fit for each studied system, proving the reliability of the obtained values of the single-crystal elastic constants (C_{ij}s).

(b) According to Pugh's empirical criterion [41], a material is malleable if the B/G ratio is greater than 1.75; otherwise, it is fragile. The calculated B/G ratio values; listed in Table 5, classify the title systems as ductile materials. Ductile materials are resistant to thermal shocks.

(c) Debye temperature θ_D can be derived from the isotropic polycrystalline elastic moduli B and G using the known relationships [42]. As a rule, a high value of θ_D implies a high thermal conductivity and high associated melting temperature. The calculated θ_D values of for the studied compounds are listed in Table 5.

Table 6
Sound velocities (in ms^{-1}) along the [100], [110] and [111] crystallographic directions for $ZnRh_2O_4$ and $CdRh_2O_4$ calculated from the elastic constants obtained using Chapin and Morteza methods [24].

System	V_l^{100}	V_t^{100}	V_l^{110}	V_{t1}^{110}	V_{t2}^{110}	V_l^{111}	v_T^{111}
$ZnRh_2O_4$							
Chapin	6372	3048	6442	3048	2896	6466	2948
Morteza	6442	3072	6540	3072	2857	6573	2931
$CdRh_2O_4$							
Chapin	5479	2653	5751	2653	1996	5839	2236
Morteza	5646	2653	5871	2653	2109	5944	2305

(iv) Evaluation of the elastic anisotropy extent in materials is of a great interest due to its implication in engineering science as well as in crystal physics. Indeed, the elastic anisotropy is highly correlated with the possibility to induce microcracks in materials [43] and has a significant influence on the nanoscale precursor textures in alloys [44]. Two different approaches were used to quantify the elastic anisotropy of the title compounds in the present work.

1. A universal index A^U, defined as follows [45]: $A^U = 5\frac{G_V}{G_R} + \frac{B_V}{B_R} - 6$, where B_V (G_V) and B_R (G_R) represent the Voigt and Reuss estimations of B (G), respectively, is widely used to measure the elastic anisotropy extent in crystals. For an isotropic single crystal, A^U is equal to zero. Thus, the deviation of the magnitude of A^U from zero measures the degree of the elastic anisotropy in the considered crystal. From Morteza method C_{ij}s, we found that A^U is equal to 0.025 for $ZnRh_2O_4$ and 0.257 for $CdRh_2O_4$, indicating that $ZnRh_2O_4$ is characterized by a weak elastic anisotropy while $CdRh_2O_4$ is characterized by a noticeable one.
2. A very practical way to estimate the elastic anisotropy in a material is by visualizing the dependence of its elastic moduli on the crystallographic directions. In an isotropic system, the 3D closed surface representing the dependence of the elastic modulus on the crystallographic directions should exhibit a spherical shape. Thus, the magnitude of the deviation of the 3D-representation of the crystallographic direction dependence of the elastic modulus from the spherical shape gives the extent of the elastic anisotropy. The crystallographic direction dependence of the Young's modulus E of a cubic crystal is given by the following relationship [46]:

$$E^{-1} = S_{11} - (2S_{11} - 2S_{12} - S_{44})(l_1^2 l_2^2 + l_1^2 l_3^2 + l_2^2 l_3^2)$$

S_{ij}s are the components of the elastic compliance matrix, l_1, l_2 and l_3 are the directional cosines with respect to the *x*-, *y*- and *z*-axes, respectively. Fig. 7 shows that the 3D-representation of the crystallographic direction dependence of the Young's modulus of $ZnRh_2O_4$ deviates slightly from the spherical shape, indicating that this compound is characterized by a weak elastic anisotropy, while that of $CdRh_2O_4$ deviates noticeably from the spherical shape, revealing that this compound is characterized by a considerable elastic anisotropy. For more clear visualization of the elastic anisotropy, the cross-sections of the 3D closed surfaces in the [001] plane of the examined compounds are also shown in Fig. 7. One can note that the deviation of the cross section from the circle is slight for $ZnRh_2O_4$, indicting its low elastic anisotropy, whereas this deviation is considerable for $CdRh_2O_4$, indicating the high elastic anisotropy of $CdRh_2O_4$.

3.5. Thermoelectric properties

Thermoelectric materials (TE) efficiently convert heat to

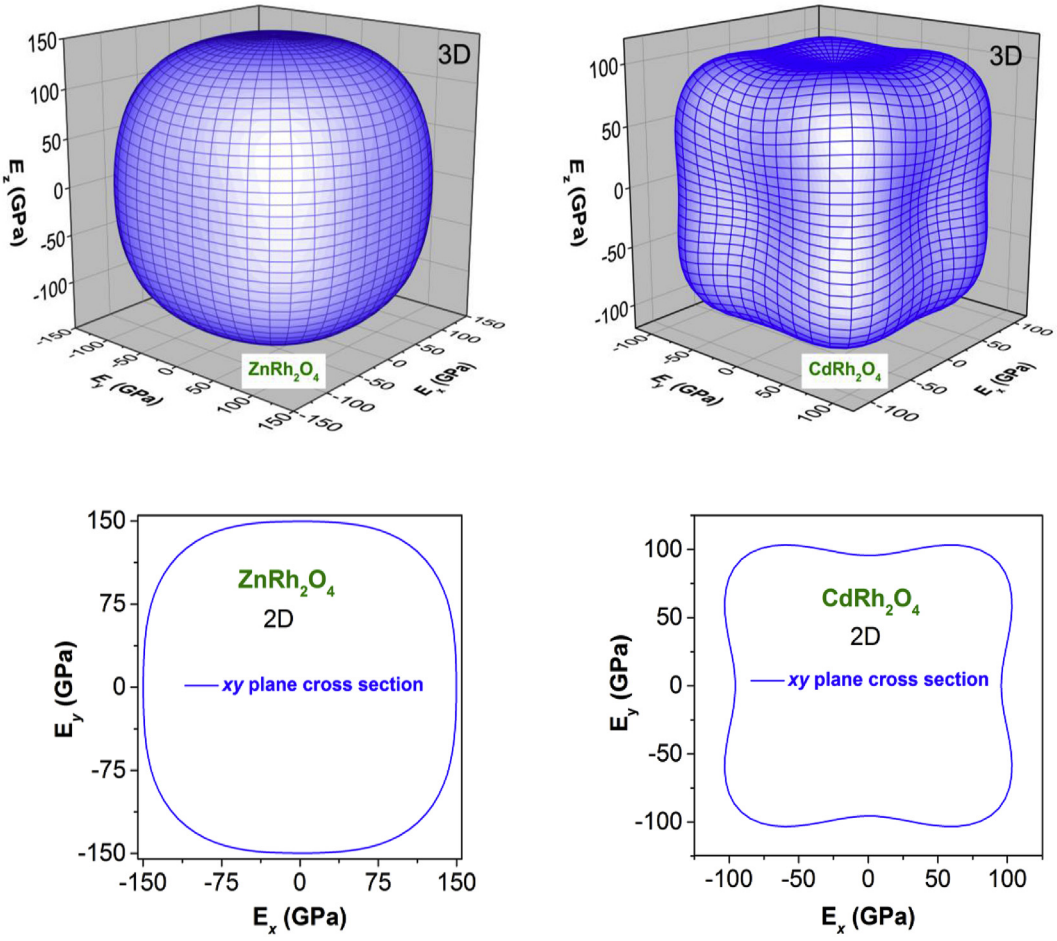

Fig. 7. 3D closed surface representation of the directional dependence of the Young's modulus (in GPa) (upper panels) and their projections on the (001) (*xy*) plane for $ZnRh_2O_4$ and $CdRh_2O_4$.

electricity and thereby are of great interest for energy applications. The thermoelectric performance of TE is characterized by a dimensionless parameter called figure of merit *ZT* defined as $ZT = S^2\sigma/(k_e + k_l)$, where *S*,σ, *T*, κ_e and κ_l are the Seebeck coefficient (called also thermopower), electrical conductivity, absolute temperature, electronic thermal conductivity and lattice thermal conductivity, respectively. A high *ZT* requires a combination of high electrical conductivity with low thermal conductivity and high Seebeck coefficient. Though there is no theoretical upper limit of *ZT*, it is challenging to achieve higher values because the three conflicting transport parameters *S*, σ and κ[47]. Therefore, an efficient TE can be designed by optimizing its thermoelectric parameters *S*, σ and κ. Fig. 8 illustrates the charge-carrier concentration dependence of the Seebeck coefficient (*S*), electrical conductivity scaled by relaxation time (σ/τ), electronic thermal conductivity scaled by relaxation time (k_e/τ), power factor ($PF = S^2\sigma/\tau$) and the thermoelectric figure of merit $ZT_e = S^2\sigma T/k_e$ for both the *n*-type and *p*-type doped $ZnRh_2O_4$ and $CdRh_2O_4$ compounds at three fixed temperatures, namely T: 300, 600 and 900 K. We have investigated the transport properties of the considered compounds for a charge-carrier concentration between 10^{17} cm^{-3} and 10^{21} cm^{-3}, which is an optimum charge-carrier concentration range for better thermoelectric performance. Fig. 8 shows that the magnitude of Seebeck coefficient *S* decreases with increasing carrier concentration and increases with increasing temperature for both the *n*-type and *p*-type doped compounds. This is a common trend in the thermoelectric materials. One can note that at the same temperature and charge-carrier concentration, the magnitude of *S* for the *p*-doped system is larger than that of the *n*-doped one throughout the studied charge-carrier concentration range. This might be because

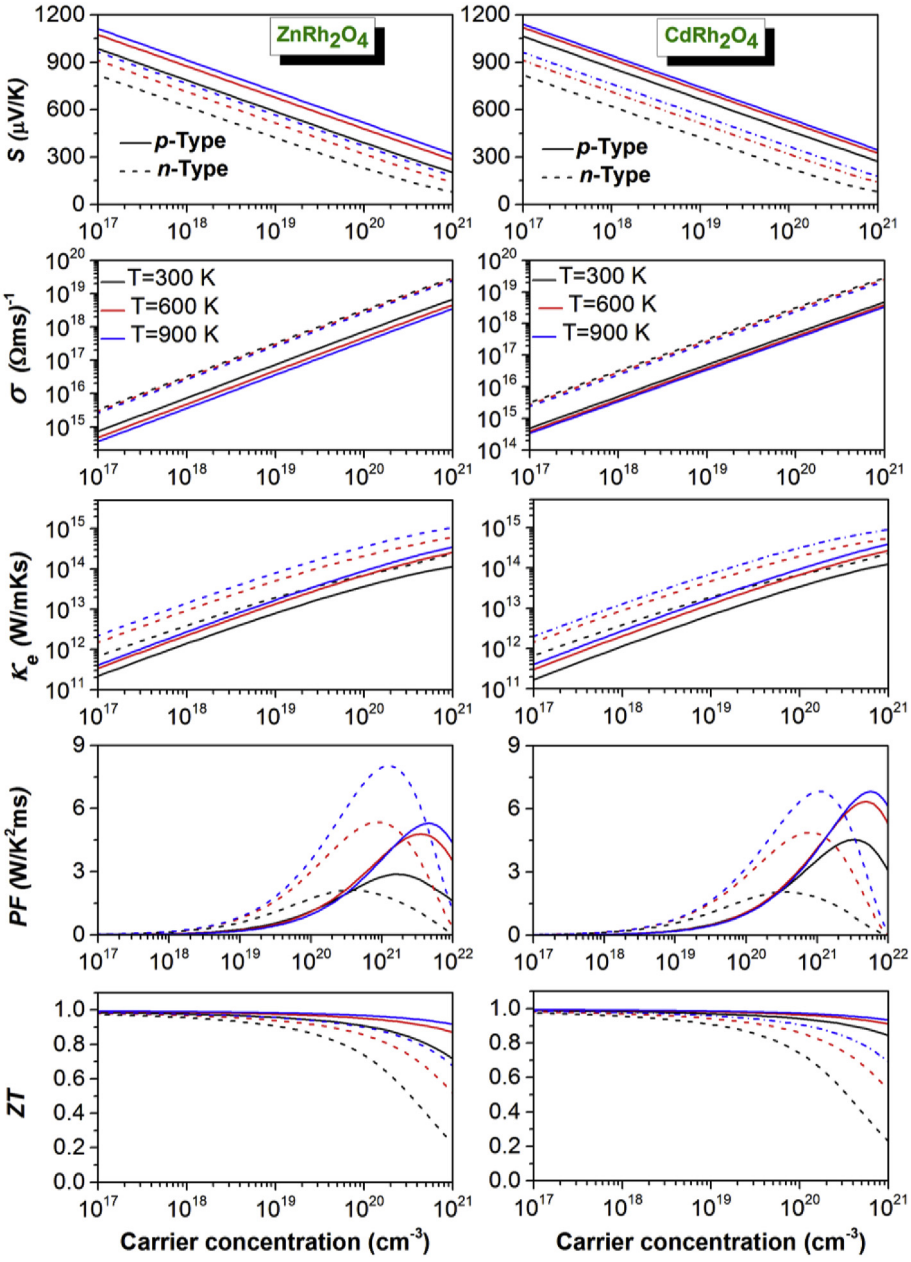

Fig. 8. Variation of the Seebeck coefficient (*S*), electrical conductivity over relaxation time (σ/τ), electronic thermal conductivity over relaxation time (k_e/τ), power factor (*PF*) and figure of merit (ZT_e) as functions of charge-carrier concentration for the *n*-type and *p*-type doping $ZnRh_2O_4$ and $CdRh_2O_4$ for different fixed temperatures.

the valence bands at the VBM are less dispersive than the conduction bands at the CBM, i.e., the hole effective mass at the VBM is larger than the electron one at the CBM. Thus, one can expect that the *p*-type doped $ZnRh_2O_4$ and $CdRh_2O_4$ are more favourable for thermoelectric performance than the *n*-type doped ones. The thermopower *S* shows practically the same behavior regarding the variation of carrier concentration and temperature for the two studied oxide spinels. This behavior might be attributed to the similarity of their energy band dispersions around the Fermi level. For both studied compounds, the electrical and electronic thermal conductivities scaled by relaxation time (σ/τ and k_e/τ) increase with increasing carrier concentration for both holes and electrons. At the same temperature and charge-carrier concentration, the electrical and thermal conductivities of the electrons are larger than those of the holes for both investigated compounds. This result is expected because the hole effective masses at the VBM are larger than those of the electrons at the CBM. At the same temperature and charge-carrier concentration, the maximum figure of merit (*ZT*) of the hole-doped systems are slightly larger than that of the electron-doped ones. The figure of merit ZT_e reaches a maximum of approximately 1 for a hole concentration of $1 \times 10^{17} cm^{-3}$. To shed light on the quality of the thermopower *S* of $ZnRh_2O_4$ and $CdRh_2O_4$, we compared the values of their Seebeck coefficients with that of the bismuth telluride alloy Bi_2Te_3, a traditional thermoelectric material. At $T = 300$ K and charge-carrier concentration of $4 \times 10^{18} cm^{-3}$, the Seebeck coefficient *S* is equal to 313 μVK^{-1} for the *p*-type Bi_2Te_3 and to $-196\ \mu VK^{-1}$ for the *n*-type one [48]. Under the same conditions, *S* is equal to 667 (745) μVK^{-1}

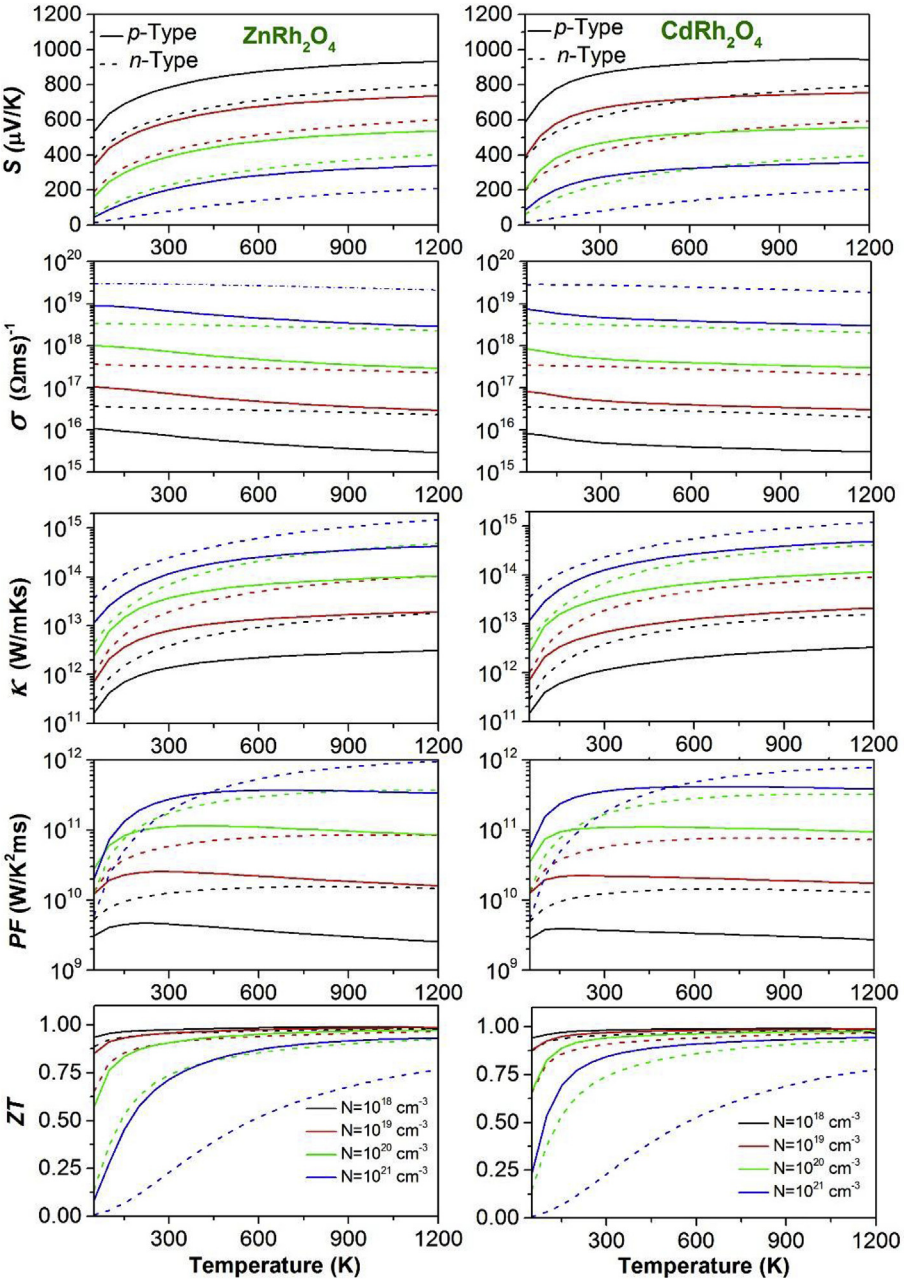

Fig. 9. Variation of the Seebeck coefficient (*S*), electrical conductivity over relaxation time (σ/τ), electronic thermal conductivity over relaxation time (k_e/τ), power factor (*PF*) and figure of merit (ZT_e) as functions of temperature for the *n*-type and *p*-type doping $ZnRh_2O_4$ and $CdRh_2O_4$ for different fixed charge-carrier concentrations.

for the *p*-type $ZnRh_2O_4$ ($CdRh_2O_4$) and −501 (−502) μVK^{-1} for the *n*-type one. Therefore, one can appreciate that the Seebeck coefficients of $ZnRh_2O_4$ and $CdRh_2O_4$ are greater than that of the traditional thermoelectric compound Bi_2Te_3. So, one can claim that the spinel oxides $ZnRh_2O_4$ and $CdRh_2O_4$ are potential candidates for thermoelectric applications if one can further reduce their thermal conductivities via some techniques, such as alloying, nanostructuring, or superlattice growth.

To explore the temperature effect on the thermoelectric properties of the title compounds, temperature dependence of the Seebeck coefficient, electrical and thermal conductivities scaled by relaxation time and figure of merit were calculated for both *n*-type and *p*-type compounds at fixed charge-carrier concentrations (1×10^{18} cm^{-3}, 1×10^{19} cm^{-3}, 1×10^{20} cm^{-3} and 1×10^{21} cm^{-3}). From Fig. 9, one can note that for a charge-carrier concentration fixed at 1×10^{18} cm^{-3}, the thermoelectric performance of the considered compounds practically does not vary with temperature over a wide temperature range.

3.6. Thermodynamical properties

Thermodynamic properties of the spinel oxides XRh_2O_4 (X = Zn, Cd], including pressure and temperature dependences of the lattice parameter, bulk modulus, volume expansion coefficient, isochoric and isobaric heat capacities and Debye temperature, were investigated via the quasi-harmonic Debye model as implemented in the Gibbs program [49]. Theoretical details of the quasi-harmonic Debye model are available in Ref. [49].

Temperature dependence of the lattice parameter (*a*) and bulk modulus (B) for the XRh_2O_4 (X = Zn, Cd] spinels at some fixed pressures (0, 5, 10, 15 and 20 GPa) are depicted in Fig. 10. B and *a* are nearly constant for temperature lower than 100 K. For temperature higher than 100 K, B decreases and *a* increases with increasing temperature at a fixed pressure, while B increases and *a* decreases with increasing pressure at a fixed temperature. One can note that the increase propensity of the lattice parameter with temperature slightly decreases with increasing pressure. The effect of increasing pressure on the lattice parameter and bulk modulus is the same as that of decreasing temperature. At zero pressure and ambient temperature, B (*a*) is approximately equal to 181 GPa (10.1767 Å) in $ZnRh_2O_4$ and 173 GPa (10.4881 Å) in $CdRh_2O_4$.

Fig. 11 shows the temperature dependence of the volume thermal expansion coefficient (α) at some fixed pressures (0, 5, 10, 15 and 20 GPa) for $ZnRh_2O_4$ and $CdRh_2O_4$. For temperature $T < 200\ K$, α increases sharply with increasing temperature at a fixed pressure, especially at zero pressure. For temperature $T > 200\ K$, the propensity of increase of α becomes weaker and it gradually tends to a linear increase except for zero pressure. The volume thermal expansion coefficient decreases strongly with increasing pressure. From Fig. 11, one can observe that for P = 20 GPa and T > 200 K, the expansion coefficient increases very slowly with increasing temperature, which means that under high pressure the effect of temperature on α is suppressed. At zero pressure and room temperature, α is approximately equal to 4.64×10^{-5} K^{-1} in $ZnRh_2O_4$ and 4.32×10^{-5} K^{-1} in $CdRh_2O_4$.

Fig. 12 shows the temperature dependence of the isochoric (C_V) and isobaric (C_P) heat capacities at some fixed pressures (0, 5, 10, 15 and 20 GPa). At low temperature ($T < 150\ K$), C_P and C_V are proportional to T^3 in agreement with the standard elastic continuum theory [50]. The difference between C_P and C_V is very slight. Both C_V and C_P increase with increasing temperature at a given pressure and decrease as pressure rises at a given temperature. For temperature lower than 400 K, C_V and C_P increase sharply with increasing temperature. For temperature higher than 400 K, the increase of C_V gradually slows and it tends to the Dulong-Petit limit (349.21 $Jmol^{-1}K^{-1}$), indicating that all the phonon modes are excited. The variation feature of the C_P is similar to that of C_V in the low temperature region, both of them are increasing with temperature; this is due to the anharmonic approximations. However, in the high temperature range, the anharmonic effect on C_V is

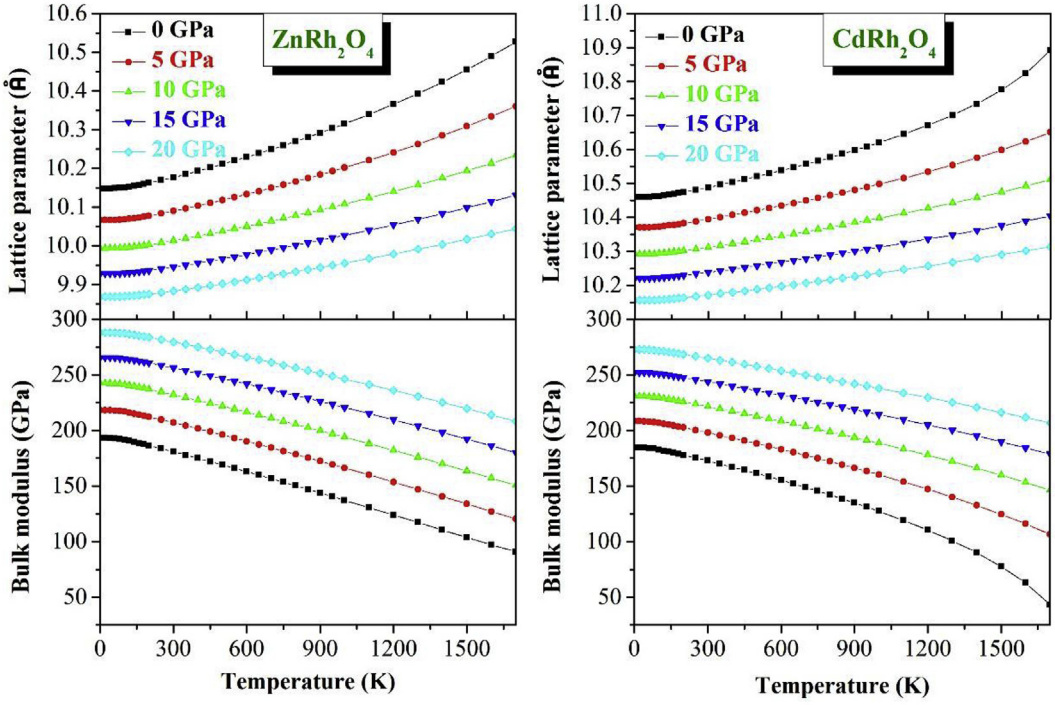

Fig. 10. Lattice constant and bulk modulus versus temperature at some fixed pressures for the $ZnRh_2O_4$ and $CdRh_2O_4$ spinels.

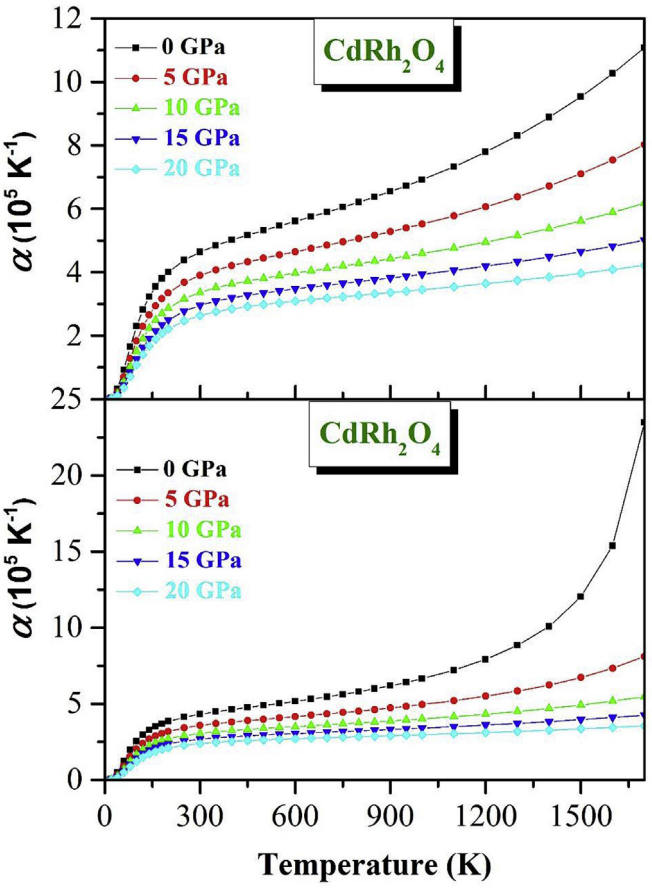

Fig. 11. Thermal expansion coefficient versus temperature at some fixed pressures for the $ZnRh_2O_4$ and $CdRh_2O_4$ spinels.

suppressed, the change tendency of C_P exhibits apparently different features; it increases with increasing temperature and do not converge to a constant value. From Fig. 12, one can note that temperature and pressure have opposite influences on the heat capacity and the effect of temperature on the heat capacity is more significant than that of pressure. The value of C_V (C_P) at 300 K and zero pressure is 319.21 $Jmol^{-1}K^{-1}$ (330.19 $Jmol^{-1}K^{-1}$) for $ZnRh_2O_4$ and 327.94 $Jmol^{-1}K^{-1}$ (337.90 $mol^{-1}K^{-1}$) for $CdRh_2O_4$.

Debye temperature is a fundamental thermodynamical parameter that is directly related to many physical properties of solids, such as elastic constants, melting temperature and specific heat. Temperature dependence of Debye temperature θ_D at some fixed pressures (0, 5, 10, 15 and 20 GPa) is displayed in Fig. 13. Debye temperature θ_D is nearly constant in the 0–100 K range and then decreases with increasing temperature. The propensity of the increase of θ_D decreases with increasing pressure. Calculated θ_D at zero pressure and temperature is equal to 414.5 K for $ZnRh_2O_4$ and 345.3 K for $CdRh_2O_4$. It is worth to note that the $ZnRh_2O_4$ and $CdRh_2O_4$ Debye temperature values calculated using the quasi-harmonic Debye model are in good agreement with the corresponding ones derived from the elastic constants (450 K for $ZnRh_2O_4$ and 348 K for $CdRh_2O_4$). This might be an indication that the quasi-harmonic Debye model is a very reasonable alternative to account for the thermal effects with no expensive task in terms of computational time.

4. Conclusions

In summary, the structural, electronic, optical, elastic, thermoelectric and thermodynamic properties of the XRh_2O_4 (X = Zn, Cd) oxide spinels were studied using the full potential linearized augmented plane wave plus local orbitals (FP-LAPW+lo) approach within the framework of density functional theory. The optimized structural parameters of the title compounds obtained using the GGA-PBEsol to model the exchange-correlation energy are in

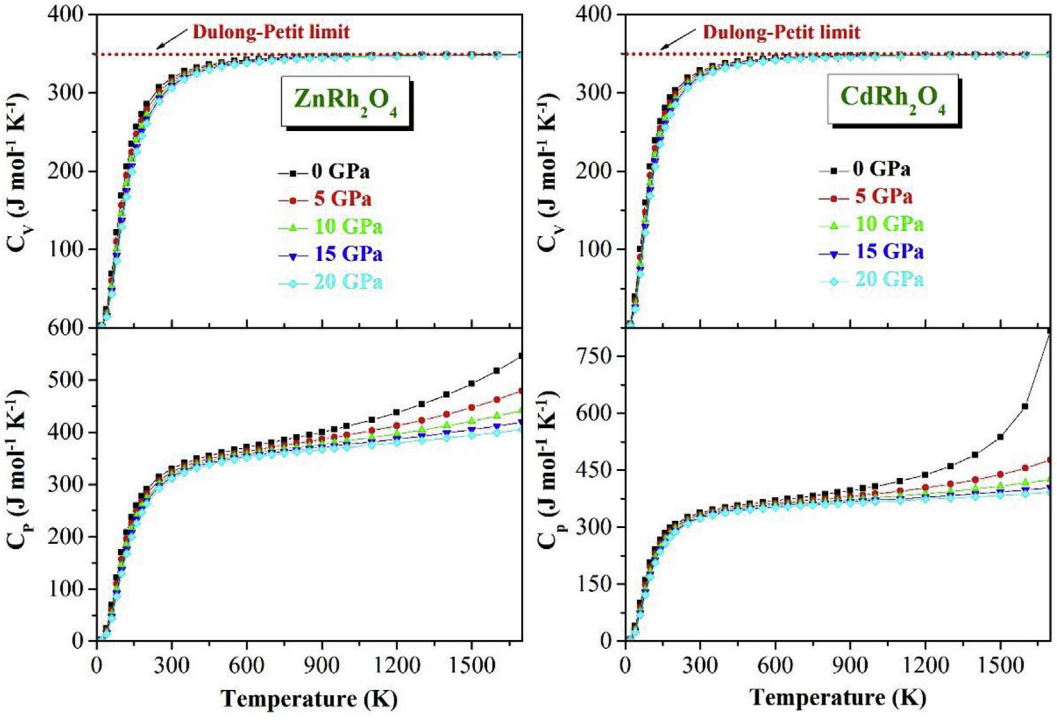

Fig. 12. Temperature dependence of the constant volume heat capacity (C_V) and constant pressure heat capacity (C_p) at some fixed pressures for the $ZnRh_2O_4$ and $CdRh_2O_4$ spinels.

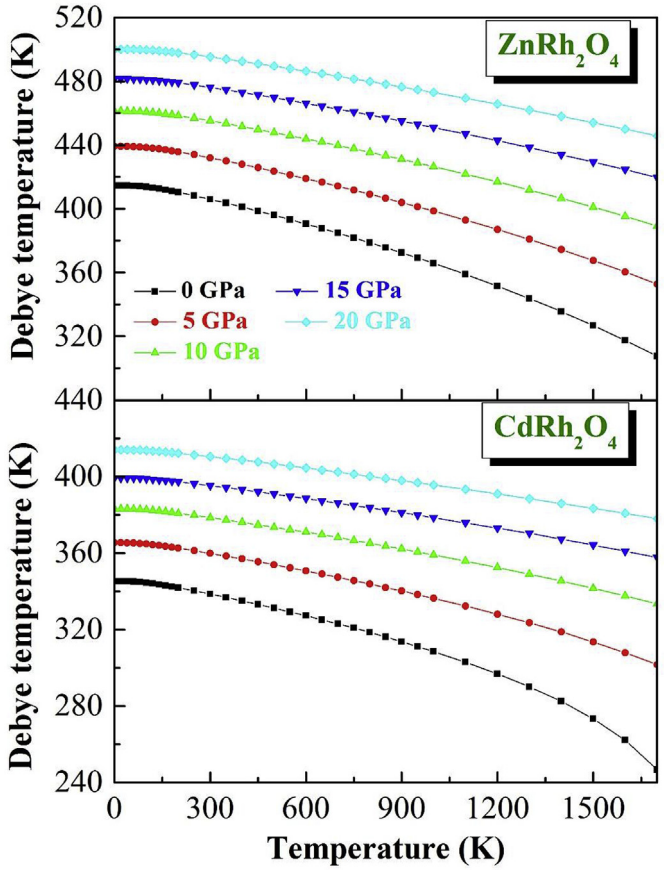

Fig. 13. Debye temperature θ_D versus temperature at some fixed pressures for the $ZnRh_2O_4$ and $CdRh_2O_4$ spinels.

excellent agreement with the available experimental data. The calculated band structures reveal that both studied compounds are indirect band gap semiconductors. The calculated $ZnRh_2O_4$ band gap using the TB-mBJ is in good agreement with the available experimental data. Analysis of the DOS diagrams reveals that the origin of the band gap in the XRh_2O_4 (X = Zn, Cd) spinels is due to the ligand field splitting of the Rh-4d into fully occupied $Rh:4d-t_{2g}^6$ and empty levels $Rh:4d-e_g^0$. The calculated charge-carrier effective masses show that the valence band holes are heavier than the conduction band electrons. Linear optical functions, including dielectric function, refractive index, extinction coefficient, reflectivity, absorption coefficient, energy-loss function were calculated, and the critical points in the optical spectra are assigned to the electronic interband transitions according to the calculated band structure. It is found that the occupied $Rh:4d-t_{2g}^6$ states and the empty states $Rh:4d-e_g^0$ play the major role in the optical transitions as initial and final states, respectively. The electronic and optical spectra of the two considered compounds have rather similar shapes. There are no available experimental data for the elastic properties of the title materials, so our results are pure theoretical predictions. The agreement between the calculated elastic constants using two different methods could prove the reliability of the reported results. The predicted elastic moduli suggest that the examined spinels are mechanically stable and ductile materials. $ZnRh_2O_4$ exhibits a weak elastic anisotropy while $CdRh_2O_4$ demonstrates a noticeable elastic anisotropy. The elastic wave velocities and Debye temperature are numerically estimated from the calculated elastic constants. Charge-carrier concentration dependence of the thermoelectric parameters, including the Seebeck coefficient, electronic conductivity, thermal conductivity and figure of merit, was explored. The calculated Seebeck coefficient values demonstrate that the *p*-type title compounds are more favourite for thermoelectric performance than the *n*-type ones. The obtained results suggest that the spinel oxides $ZnRh_2O_4$ and $CdRh_2O_4$ are potential candidates for thermoelectric applications if one can further reduce their thermal conductivities via some techniques.

Acknowledgment

The authors (A. Bouhemadou and S. Bin-Omran) extend their appreciation to the International Scientific Partnership Program ISPP at King Saud University for funding this research work through ISPP# 0025.

References

[1] T. Minami, Transparent conducting oxide semiconductors for transparent electrodes, Semicond. Sci. Technol. 20 (2005) S35–S44.
[2] D.O. Scanlon, G.W. Watson, Band gap anomalies of the ZnM2IIIO4 (MIII=Co, Rh, Ir) spinels, Phys. Chem. Chem. Phys. 13 (2011) 9667–9675.
[3] R.G. Gordon, Criteria for choosing transparent conductors, MRS Bull. 25 (2011) 52–57.
[4] N. Mansourian-Hadavi, S. Wansorm, N.H. Perry, A.R. Nagaraja, T.O. Mason, Transport and band structure studies of crystalline ZnRh2O4, Phys. Rev. B 81 (2010), pp. 075112-1-6.
[5] H. Mizoguchi, M. Hirano, S. Fujitsu, T. Takeuchi, K. Ueda, H. Hosono, $ZnRh_2O_4$: a p-type semiconducting oxide with a valence band composed of a low spin state of Rh3+ in a 4d6 configuration, Appl. Phys. Lett. 80 (2002) 1207–1209.
[6] H. Ohta, H. Mizoguchi, M. Hirano, S. Narushima, T. Kamiya, H. Hosono, Fabrication and characterization of heteroepitaxial p-n junction diode composed of wide-gap oxide semiconductors p-ZnRh2O4/n-ZnO, Appl. Phys. Lett. 82 (2003) 823–825.
[7] H. Ohta, K. Nomura, H. Hiramatsu, K. Ueda, T. Kamiya, M. Hirano, H. Hosono, Frontier of transparent oxide semiconductors, Solid State Electron. 47 (2003) 2261–2267.
[8] X. Wang, Y. Guo, Y. Sun, K. Yamaura, Metal-insulator transition in Na-doped post spinel CdRh2O4, J. Alloys Compd. 563 (2013) 119–123.
[9] M. Dekkers, G. Rijnders, D.H.A. Blank, ZnIr2O4, a p-type transparent oxide semiconductor in the class of spinel zinc-d6-transition metal oxide, Appl. Phys. Lett. 90 (2007), pp. 021903-1-3.
[10] A. Banerjee, Z. Singh, V. Venugopal, Heat capacity and Gibbs energy of formation of the ternary oxide CdRh2O4, Solid State Ionics 180 (2009) 1337–1341.
[11] X. Wang, Y. Guo, Y. Shi, A.A. Belik, Y. Tsujimoto, W. Yi, Y. Sun, Y. Shirako, M. Arai, M. Akaogi, Y. Matsushita, K. Yamaura, High-pressure synthesis, crystal structure, and electromagnetic properties of CdRh2O4: an analogous oxide of the postspinel mineral $MgAl_2O_4$, Inorg. Chem. 51 (2012) 6868–6875.
[12] S.Zh. Karazhanov, P. Ravindran, Ab initio study of double oxides ZnX2O4 (X=Al, Ga, In) having spinel structure, J. Am. Ceram. Soc. 93 (2010) 3335–3341.
[13] H. Dixit, N. Tandon, S. Cottenier, R. Saniz, D. Lamoen, B. Partoens, V. Van Speybroeck, M. Waroquier, Electronic structure and band gap of zinc spinel oxides beyond LDA: $ZnAl_2O_4$, $ZnGa_2O_4$ and $ZnIn_2O_4$, New J. Phys. 13 (2011), pp. 063002-1-11.
[14] G.B. Wilson-Short, D.J. Singh, M. Fornari, M. Suewattana, Thermoelectric properties of rhodates: layered β-SrRh2O4 and spinel ZnRh2O4, Phys. Rev. B 75 (2007) 03512–03513.
[15] L. Guo, S.T. Zhang, W.J. Feng, G. Hu, A first-principles study on the structural, elastic, electronic, and optical properties of CdRh2O4, J. Mater. Sci. 49 (2014) 1205–1214.
[16] S. Samantha, Study of systematic trends in electronic and optical properties within ZnM_2O_4 (M = Co, Rh, Ir) family by FPLAPW method within PBE and TB-mBJ potentials, Opt. Mater. 45 (2015) 141–147.
[17] M.N. Amini, H. Dixit, R. Saniz, D. Lamoen, B. Partoens, The origin of p-type conductivity in ZnM2O4 (M=Co, Rh, Ir) spinels, Phys. Chem. Chem. Phys. 16 (2014) 2588–2596.
[18] D. Allali, A. Bouhemadou, S. Bin-Omran, Theoretical prediction of the structural, electronic and optical properties of SnB2O4 (B = Mg, Zn, Cd), Comput. Mater. Sci. 51 (2012) 194–205.
[19] D. Allali, A. Bouhemadou, E. Muhammad Abud Al Safi, S. Bin-Omran, M. Chegaar, R. Khenata, A.H. Reshak, Electronic and optical properties of the SiB2O4 (B=Mg, Zn, and Cd) spinel oxides: an ab initio study with the Tran–Blaha-modified Becke–Johnson density functional, Phys. B Condens. Matter 443 (2014) 24–34.
[20] H. Dixit, R. Saniz, S. Cottenier, D. Lamoen, B. Partoens, Electronic structure of transparent oxides with the Tran–Blaha modified Becke–Johnson potential,

J. Phys. Condens. Matter 24 (2012), pp. 205503-1-9.
[21] R.H. Arlett, Growth of $ZnRh_2O_4$ crystals, J. Am. Ceram. Soc. 51 (1968) 292–293.
[22] R.P. Agarwala, Structure of cadmium rhodite, CdRh2O4, J. Inorg. Gen. Chem. 307 (1961) 205–207.
[23] S. Cottenier, Density Functional Theory and the Family of (L)APW-methods: a Step-by-step Introduction, second ed., 2002-2013. ISBN 978-90-807215-1-7 (freely available at: http://www.wien2k.at/reg user/textbooks.
[24] P. Blaha, K. Schwarz, G. Madsen, D. Kvasnicka, J. Luitz, An Augmented Plane Wave Plus Local Orbitals Program for Calculating Crystal Properties, Vienna University of Technology, Institute of Materials Chemistry Getreidemarkt, Vienna, Austria, 2017, 9/165-TC A-1060.
[25] J.D. Pack, H.J. Monkhorst, Special points for Brillouin-zone integrations, Phys. Rev. B 16 (1977) 1748–1749.
[26] J.P. Perdew, A. Ruzsinszky, G.I. Csonka, O.A. Vydrov, G.E. Scuseria, L.A. Constantin, X. Zhou, K. Burke, Restoring the density-gradient expansion for exchange in solids and surfaces, Phys. Rev. Lett. 100 (2008), pp. 136406-1-4.
[27] A.D. Becke, E.R. Johnson, A simple effective potential for exchange, J. Chem. Phys. 124 (2006), pp. 221101-1-4.
[28] F. Tran, P. Blaha, K. Schwarz, Band gap calculations with Becke–Johnson exchange potential, J. Phys. Condens. Matter 19 (2007) 1962081–1962088.
[29] F. Tran, P. Blaha, Accurate band gaps of semiconductors and insulators with a semilocal exchange-correlation potential, Phys. Rev. Lett. 102 (2009), pp. 226401-1-4.
[30] D. Koller, F. Tran, P. Blaha, Merits and limits of the modified Becke-Johnson exchange potential, Phys. Rev. B 83 (2011), pp. 195134-1-10.
[31] D. Koller, F. Tran, P. Blaha, Merits and limits of the modified Becke-Johnson exchange potential, Phys. Rev. B 83 (2011), pp. 195134-1-10.
[32] D. Koller, F. Tran, P. Blaha, Band gaps from the Tran-Blaha modified Becke-Johnson approach: a systematic investigation, Phys. Rev. B 85 (2012), pp. 155109-1-8.
[33] Kin Mun Wong, Wilayat Khan, M. Shoaib, Umar Shah, Shah Haider Khan, G. Murtaza, *Ab initio* investigation of the structural, electronic and optical properties of the $Li_2In_2XY_6$ (X = Si, Ge; Y = S, Se) compounds, J. Electron. Mater. 47 (2018) 566–576.
[34] G.K. Madsen, D.J. Singh, BoltzTraP. A code for calculating band-structure dependent quantities, J. Comput. Phys. Commun. 175 (2006) 67–71.
[35] T. Fang, S. Zheng, T. Zhou, H. Chen, P. Zhang, Validity of rigid-band approximation in the study of thermoelectric properties of *p*-type FeNbSb-based half-Heusler compounds, J. Electron. Mater. 46 (2017) 3030–3035.
[36] F.D. Murnaghan, The compressibility of media under extreme pressures, Proc. Natl. Acad. Sci. U.S.A. 30 (1944) 244–247.
[37] J.P. Perdew, K. Burke, M. Ernzerhof, Generalized *gradient approximation made simple*, Phys. Rev. Lett. 77 (1996) 3865–3868.
[38] J.P. Perdew, A. Zunger, Self-interaction correction to density-functional approximations for many-electron systems, Phys. Rev. B 23 (1981) 5048–5079.
[39] D.R. Penn, Wave-number-dependent dielectric function of semiconductors, Phys. Rev. 128 (1960), 2093-1-5.
[40] M.H. Born, Dynamical Theory of Crystal Lattices, Clarendo, Oxford, 1956.
[41] S.F. Pugh, Relations between the elastic moduli and the plastic properties of polycrystalline pure metals, Phil. Mag. 45 (1954) 823–843.
[42] O.L. Anderson, A simplified method for calculating the Debye temperature from elastic constants, J. Phys. Chem. Solids 24 (1963) 909–917.
[43] P. Ravindran, L. Fast, P.A. Korzhavyi, B. Johansson, O. Eriksson, J. Appl. Phys. 84 (1998) 4891.
[44] P. Lloveras, T. Castán, M. Porta, A. Planes, A. Saxena, Phys. Rev. Lett. 100 (2008), 165707.
[45] S.I. Ranganathan, M. Ostoja-Starzewski, Universal elastic anisotropy index, Phys. Rev. Lett. 101 (2008), 55504-1-4.
[46] J.F. Nye, Properties of Crystals, Oxford University Press, 1985.
[47] M.K. Yadav, B. Sanyal, First-principles study of thermoelectric properties of Li-based half-Heusler alloys, J. Alloys Compd. 622 (2015) 388–393.
[48] S. Mishra, S. Satpathy, O. Jepsen, Electronic structure and thermoelectric properties of bismuth telluride and bismuth selenide, J. Phys. Condens. Matter 9 (1997) 461–470.
[49] M.A. Blanco, E. Francisco, V. Luaña, Comput. Phys. Commun. 158 (2004) 57.
[50] P. Debye, The theory of specific heat, Ann. Phys. 39 (1912) 789–839.